

Reconstruction of Cardiac Cine MRI under Free-breathing using Motion-guided Deformable Alignment and Multi-resolution Fusion

Xiaoxiang Han¹, Qiaohong Liu^{2,*}, Yiman Liu^{3,4}, Keyan Chen¹, Yuanjie Lin¹, Weikun Zhang¹

¹School of Health Science and Engineering, University of Shanghai for Science and Technology, Shanghai, 200093, P.R.China

^{2*}School of Medical Instruments, Shanghai University of Medicine and Health Sciences, Shanghai, 201318, P.R.China

³Department of Pediatric Cardiology, Shanghai Children's Medical Center, School of Medicine, Shanghai Jiao Tong University, Shanghai, 200127, P.R.China

⁴Shanghai Key Laboratory of Multidimensional Information Processing, School of Communication & Electronic Engineering, East China Normal University, Shanghai, 200241, P.R.China

Corresponding Author: Qiaohong Liu, No. 279, Zhouzhu Road, Pudong New Area, Shanghai, P.R.China. Tel.: +86 137 6183 3680, Email: hqllqh@163.com

Abstract

Objective: Cardiac cine magnetic resonance imaging (MRI) is one of the important means to assess cardiac functions and vascular abnormalities. However, due to cardiac beat, blood flow, or the patient's involuntary movement during the long acquisition, the reconstructed images are prone to motion artifacts that affect the clinical diagnosis. Therefore, accelerated cardiac cine MRI acquisition to achieve high-quality images is necessary for clinical practice.

Approach: A novel end-to-end deep learning network is developed to improve cardiac cine

MRI reconstruction under free breathing conditions. First, a U-Net is adopted to obtain the initial reconstructed images in k-space. Further to remove the motion artifacts, the Motion-Guided Deformable Alignment (MGDA) method with second-order bidirectional propagation is introduced to align the adjacent cine MRI frames by maximizing spatial-temporal information to alleviate motion artifacts. Finally, the Multi-Resolution Fusion (MRF) module is designed to correct the blur and artifacts generated from alignment operation and obtain the last high-quality reconstructed cardiac images.

Main results: At an $8\times$ acceleration rate, the numerical measurements on the ACDC dataset are SSIM of $78.40\% \pm 4.57\%$, PSNR of 30.46 ± 1.22 dB, and NMSE of 0.0468 ± 0.0075 . On the ACMRI dataset, the results are SSIM of $87.65\% \pm 4.20\%$, PSNR of 30.04 ± 1.18 dB, and NMSE of 0.0473 ± 0.0072 .

Significance: The proposed method exhibits high-quality results with richer details and fewer artifacts for cardiac cine MRI reconstruction on different accelerations under free breathing conditions.

Keywords

Cardiac Cine MRI, MRI Reconstruction, Deep Learning, Motion Artifact Correction, Free Breathing

Introduction

MRI is a widely employed clinical adjunctive diagnostic tool, offering advantages such as non-invasiveness, absence of ionizing radiation, and multiple parameter acquisition. Nonetheless, due to physiological and hardware constraints, the examination speed of MRI is slower than some other imaging modalities. As an integral component of MRI technology, cine MRI can

provide the continuous assessment of organ anatomy and the physiological-pathological mechanisms in both the temporal and spatial domains. In contrast to conventional two-dimensional static MRI images, cine MRI with more crucial information in the temporal dimension is extensively applied in cardiac imaging, cine angiography, and cardiovascular disease diagnosis. Specifically for cardiac cine MRI reconstruction, the repeat acquirement of multiple heartbeat cycles spends more acquisition time which can induce patient discomfort and inevitably produce motion artifacts. Therefore, accelerated cardiac cine MRI acquisition is necessary for clinical practice.

Subsampling k-space data during MRI is the prevalent approach to reduce scanning time. However, due to the violation of Nyquist's theorem, images directly reconstructed from zero-filled under-sampled k-space data by performing Fourier inverse transform suffer from aliasing artifacts and lower SNR. In the past, numerous methods for reconstructing fully sampled MRI signals included partial Fourier transform [1], parallel imaging [2], compressed sensing (CS) [3], low-rank matrix completion [4], and manifold learning [5]. Nevertheless, traditional methods above often suffer hyper-parameter selection and slow reconstruction speed due to iterative optimization. Deep learning-based reconstruction methods have been developed to address these problems. In 2016, Wang et al. [6] pioneered the integration of deep learning into MRI reconstruction tasks. They employed convolutional neural networks to establish mappings between a large number of under-sampled images and fully sampled images. Then high-quality reconstructed images could be obtained by inputting only the under-sampled images during prediction. Subsequently, the success of this work led to the emergence of numerous deep learning-based static MRI reconstruction algorithms [7][8][9][10][11].

Although significant progress has been made in static MRI reconstruction, few recently proposed methods are oriented to dynamic MRI reconstruction based on deep learning techniques. Batchelor et al. [12] pioneered the field of motion-compensated MRI reconstruction. Odille et al. [13] used compressed sensing-based methods for dynamic cardiac MRI reconstruction under free breathing conditions. Chandarana et al. [14] applied similar techniques to reconstruct dynamic liver MRI under free-breathing conditions. Aviles-Rivero et al. [15] improved fast dynamic MRI reconstruction using multi-task optimization. Similar works refer [16][17]. The traditional CS-MRI techniques have some limitations, such as parameter selection, optimization calculation, and low acceleration factor. In contrast, deep learning-based methods have become popular in cine MRI reconstruction due to their accuracy and efficiency. For instance, Schlemper et al. [18] designed a deep cascaded CNN-based network with a data sharing (DS) layer to capture temporal correlations between different frames for cine MRI reconstruction. Qin et al. [19] proposed CRNN, which uses convolutional recurrent neural networks to handle dynamic signals and leverages bidirectional recurrent hidden connections across time series to capture spatiotemporal correlations. Küstner et al. [20] performed 3D cardiac cine MRI reconstruction based on 4D spatiotemporal convolution, but it suffered from a high computational cost. Sarasaen et al. [21] fine-tuned their network using static high-resolution MRI as prior knowledge. Additionally, some studies [22][23] consider motion information as a crucial prior in cine MRI to improve the reconstruction quality. Nevertheless, they are not specifically designed for free breathing scenarios. To this end, Eldeniz et al. [24] explored a deep learning-based reconstruction of dynamic liver MRI under free breathing conditions. Pan et al. [25] proposed a learning-based method for motion-

compensated MR reconstruction to efficiently deal with non-rigid motion corruption in cardiac MR imaging. However, the time-consuming computational cost of motion-compensated reconstruction makes it unsuitable for real-time requirements. Kunz et al. [26] developed an end-to-end model specifically for free breathing cardiac cine MRI reconstruction based on deep learning. More works refer [27][28]. Commonly, the end-to-end methods show higher computational efficiency which is more suitable for real-time requirements. Spatial-temporal information is the key to accessing dynamic image understanding. Thus, a new end-to-end network that combines the motion-guided deformable alignment module and multi-resolution fusion module is proposed for cardiac cine MRI reconstruction, aiming at taking full advantage of spatial-temporal information in consecutive MRI frames to effectively alleviate the motion artifacts and faithfully reconstruct the cardiac structure.

Materials and Methods

Problem statement

Aiming to reconstruct the fully sampled MRI data from under-sampled Cine MRI data, the problem can be formulated as follows:

$$y = M \odot Fx + \varepsilon \quad (1)$$

where x represents the fully sampled MRI data, F denotes the Fourier transform, M is the subsampling mask, \odot represents pointwise multiplication, and ε is the noise introduced during data acquisition.

To address this ill-posed inverse problem (1), deep learning is introduced to reconstruct the undersampled MRI data. The optimization formulation for this process is as follows:

$$\hat{x} = \underset{x}{\operatorname{argmin}} \frac{1}{2} \|y - M \odot Fx\|_2^2 + \lambda L(\theta) \quad (2)$$

where \hat{x} represents the reconstructed MRI data, $L(\theta)$ is the prior regularization term, and λ is the regularization coefficient. In an end-to-end deep learning framework, the optimization process of $L(\theta)$ can be expressed as follows:

$$L(\theta) = \operatorname{argmin}_{\theta} \frac{1}{2} \|x - f_{DL}(x_{zf}|\theta)\|_2^2 \quad (3)$$

where f_{DL} represents deep learning forward propagation, θ denotes the learnable parameters, and x_{zf} represents zero-filled MRI data after subsampling.

Overall architecture of the proposed method

As illustrated in Figure 1, a new end-to-end network associated with motion-guided deformable alignment (MGDA) module and multi-resolution fusion (MRF) module is proposed for free breathing cardiac cine MRI reconstruction. The proposed model comprises three main modules: the k-space signal reconstruction module, the motion-guided deformable alignment module, and the multi-resolution fusion module. Initially, the under-sampled k-space signals K_u converted from consecutive cardiac cine MR images are fed into the k-space signal reconstruction module R_u which adopts a traditional U-Net structure. The reconstructed k-space signals K_r are converted into the image domain data I_r by inverse Discrete Fourier Transform (iDFT). This process can be expressed as follows:

$$K_r = R_u(K_u) \quad (4)$$

$$I_r = iDFT(K_r) \quad (5)$$

Then, I_r is processed by the MGDA module to obtain preliminary aligned feature maps F_a . Finally, F_a is input into the MRF module for further processing to produce the final clear images. This process can be stated as:

$$F_a = MGDA(I_r) \quad (6)$$

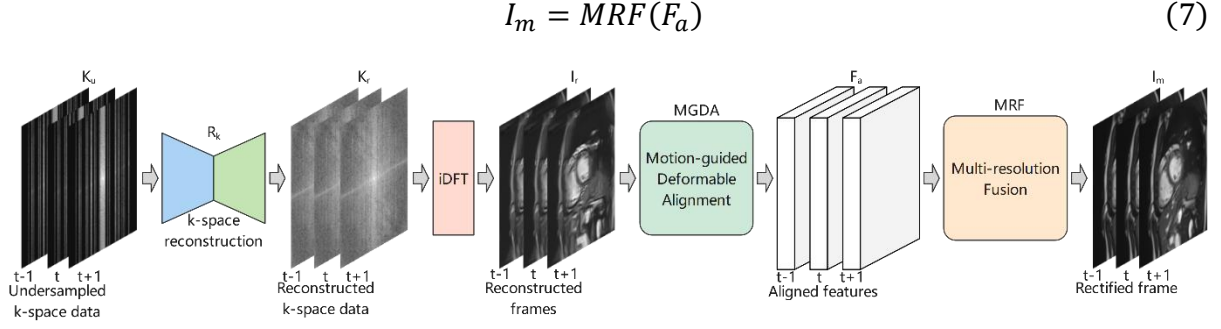


Figure 1. Overall architecture of the proposed method.

Motion-guided deformable alignment module

During the reconstruction process, cardiac and respiratory motion, together with fast-flowing blood, may cause inter-slice motion artifacts. Thus, a motion-guided deformable alignment module is introduced to alleviate the effect of motion artifacts, as depicted in Figure 2. Deformable Convolutional Networks (DCN) [30][31] are used to align the adjacent cine MRI frames to eliminate the difference between these adjacent frames and achieve the goal of artifact removal. DCN refers to the addition of an offset at the sampling position in standard convolution operations, allowing the sampling grid to deform freely. Since these offsets should be learned from preceding layer features through an additional convolutional layer, deformation occurs in a local, dense, and adaptive manner conditioned on input features [32]. However, DCNs are challenging to train, and the training process is unstable, sometimes leading to offset overflow issues [33]. Therefore, motion information from adjacent frames can be utilized to guide the learning of offsets in DCN. A typical optical flow method named SPyNet [34] is employed to achieve the motion information estimation in the proposed MGDA module. SPyNet with strong performance, low computational cost, fast processing speed, and high compatibility can effectively capture motion information at different scales by processing the images in a spatial pyramid structure. Furthermore, SPyNet uses the pre-trained weights trained

on a large-scale dataset to enhance the robustness of the proposed model. Additionally, the second-order grid propagation (SOGP) strategy [35] is adopted to aggregate more information from different spatial-temporal locations, aiming to improve the information aggregation ability in the network and the robustness of the network to occluded and fine regions.

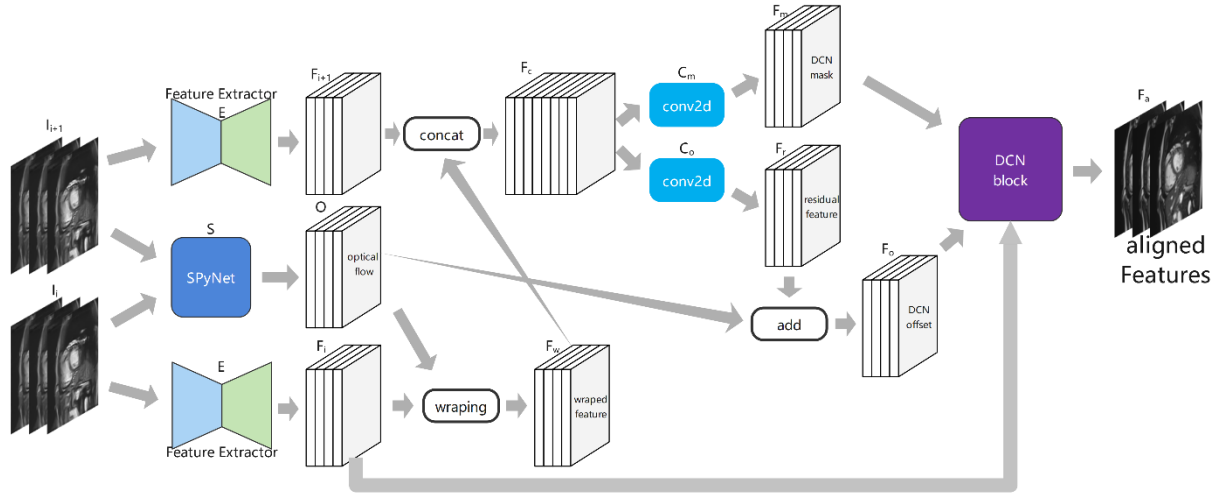


Figure 2. Motion-guided deformable alignment module.

Firstly, the reconstructed images I_i at frame i and I_{i+1} at frame $i + 1$ are fed into the feature extractor E respectively to obtain feature maps F_i and F_{i+1} . Simultaneously, I_i and I_{i+1} are input into SPyNet for optical flow estimation, resulting in an optical flow field map O . Here, E is a stacked residual block. The expressions for this process are as follows:

$$F_i = E(I_i) \quad (8)$$

$$F_{i+1} = E(I_{i+1}) \quad (9)$$

$$O = S(I_i, I_{i+1}) \quad (10)$$

where S represents SPyNet. Subsequently, F_i and O perform a warping operation to obtain distorted features F_w . Then F_w is concatenated with F_{i+1} to obtain the feature map F_c . The expressions for this process are as follows:

$$F_w = \text{Wrap}(F_i, O) \quad (11)$$

$$F_c = \text{Cat}(F_{i+1}, F_w) \quad (12)$$

where $\text{Wrap}(\cdot, \cdot)$ denotes the warping operation, which mainly involves sampling the input

features based on the deformed grid coordinates to obtain the deformed output. $Cat(\cdot, \cdot)$ represents the concatenation operation. Then, F_c is calculated by two different convolutional layers C_m and C_o to obtain the feature maps F_m and F_r , respectively. F_r and O are element-wise added to generate the feature map F_o . F_m as the DCN mask, and F_o as the DCN offset, with F_i are fed into DCN block to yield the last aligned feature map F_a . The expressions for this process are as follows:

$$F_m = C_m(F_c) \quad (13)$$

$$F_r = C_o(F_c) \quad (14)$$

$$F_o = Add(F_r, O) \quad (15)$$

$$F_a = DCN(F_i, F_o, F_m) \quad (16)$$

where $Add(\cdot, \cdot)$ denotes element-wise addition, and DCN represents the deformable convolutional network.

Multi-resolution fusion module

Although the MGDA module can effectively alleviate the motion artifacts generated from cardiac, respiratory, and fast-flowing blood motion, the accuracy of alignment is difficult to ensure when there is significant motion between adjacent cine MRI frames, which would cause some unexpected artifacts like ghosting and blurring. Further, a new multi-resolution fusion (MRF) module that considers both inter-frame and intra-frame correlations is designed to remedy this problem. The overall architecture of MRF is illustrated in Figure 3. Inspired by HRNet's [36], the proposed MRF module consists of three parallel multi-resolution subnetworks that recurrently fuse representations generated by high to low subnetworks to obtain reliable high-resolution representations. Each low-resolution subnetwork is produced from the previous high-resolution subnetwork and high-resolution subnetwork features are progressively added to the corresponding low-resolution subnetwork features to form multiple

stages with parallel connections between these multi-resolution subnetworks. Continuous exchange of information between three subnetworks through convolutional operations for multi-resolution fusion leads to richer high-resolution representations, which can effectively enhance the reconstructed details and spatial precision. Transformers [37], as a new network structure, can establish the long-range dependencies and capture temporal correlation in parallel, which benefits achieving more redundant information and enhancing the detail reconstruction. To obtain more advanced semantic information on the low-resolution subnetworks, the swin-Transformer [38] is used to capture additional global features, while simultaneously minimizing the increase of computational complexity. In the high-resolution subnetwork, the features from three different resolutions are fused to extract more effective high-level semantic features to produce the high-resolution output. Additionally, the MRF module employs 2×2 max-pooling with a stride of 2 for downsampling and $2 \times$ bilinear interpolation for upsampling.

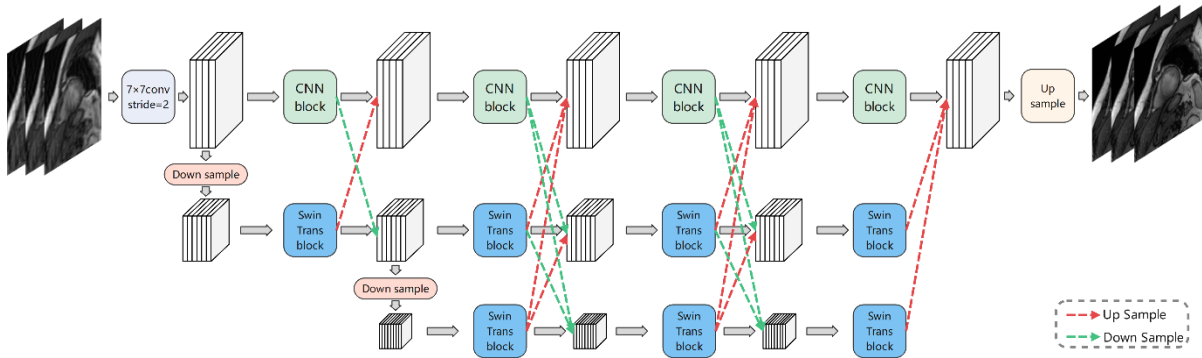


Figure 3. Multi-resolution fusion module.

Datasets

The proposed method is validated on two publicly available cine MRI datasets, namely ACDC [38] and SACMRI [39]. The ACDC dataset, designed for automated cardiac diagnosis challenges, is created using real clinical exams conducted at the University Hospital in Dijon.

It comprises 150 exams from different patients and is categorized into five classes, including

normal cases, heart failure with infarction, dilated cardiomyopathy, hypertrophic cardiomyopathy, and right ventricular abnormality. The SACMRI dataset from The Hospital for Sick Children in Toronto consists of cardiac MR images from 33 subjects.

100 patients, 20 patients, and 30 patients of the ACDC dataset are utilized for training, validation, and testing, respectively. Each subject's data includes 12 to 35 frames and 6 to 21 cardiac slice data. 26 patients, 3 patients, and 4 patients of the SACMRI dataset are used for training, validation, and testing, respectively. Each patient's data comprises 20 frames and 8 to 15 cardiac slice data. Given the availability of only magnitude images in two datasets, the method described in reference [41] is selected to synthetically generate phase maps (smoothly varying 2D sinusoid waves) on-the-fly. This approach enhances the authenticity of the simulations by eliminating the conjugate symmetry within the k-space. Variable-density 1D under-sampling masks are employed with two different acceleration factors ($4\times$ and $8\times$) to obtain the corresponding zero-filling cardiac dataset.

Implementation details

This study is implemented using Python 3.8 and PyTorch 1.12.1 on a GPU server equipped with 1 Intel Core i9-10900X CPU, 32GB RAM, and 2 Nvidia RTX3080 (10GB) GPUs. Notably, an efficient and user-friendly PyTorch-Lightning 1.7.5 framework is leveraged to simplify the coding. The batch size is set based on data dimensions to maximize memory utilization. AdamW [42] is used as an optimizer with an initial learning rate of $1e-3$ and ReduceLROnPlateau is adopted as the dynamic learning rate adjustment strategy. The model is trained for 100 epochs and the data loading program employs 16 threads. Automatic mixed precision is utilized during training and the mean squared error (MSE) loss is employed as the

loss function. The performance of cine MRI reconstruction is evaluated by the Structural Similarity Index (SSIM) [43], Peak Signal-to-Noise Ratio (PSNR), and Normalized Mean Squared Error (NMSE).

Results

The proposed method is compared with some popular Cine MRI reconstruction techniques, including kt FOCUSS [44], DC-CNN [13], CRNN [19], DRN [23], and MODRN [23]. Among these compared methods, kt FOCUSS is a compressed sensing method, while the remaining methods are based on end-to-end deep learning techniques. MODRN is an improved version of integrating motion compensation into DRN.

The quantitative comparison of all methods on the ACDC dataset is presented in Table 1. The first row displays results for under-sampled images reconstructed directly from zero-filled k-space. The proposed method outperforms other methods at both 4x and 8x acceleration rates. The proposed method achieves excellent results closest to the ground truth, with the highest PSNR and SSIM and lowest NMSE values among all the methods. Specifically, at a 4x acceleration rate, the proposed method improves 1.36% in SSIM and 0.78dB in PSNR compared with the suboptimal model MODRN. Figure 4 illustrates the boxplot of the distribution of PSNR, SSIM, and NMSE under 4 \times acceleration rate. At an 8x acceleration rate, the proposed method achieves a 1.71% improvement in SSIM and a 0.92dB improvement in PSNR compared with the suboptimal model MODRN. Figure 5 gives the boxplot of the distribution of PSNR, SSIM, and NMSE under 8 \times acceleration rate. These quantitative measurements demonstrate that the proposed method has a promising performance for different acceleration rates.

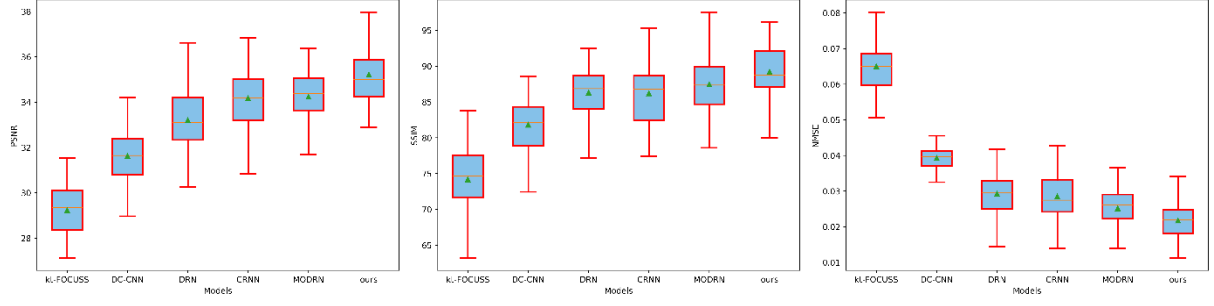


Figure 4. Boxplot of the distribution of quantitative results on the ACDC dataset under 4

\times acceleration.

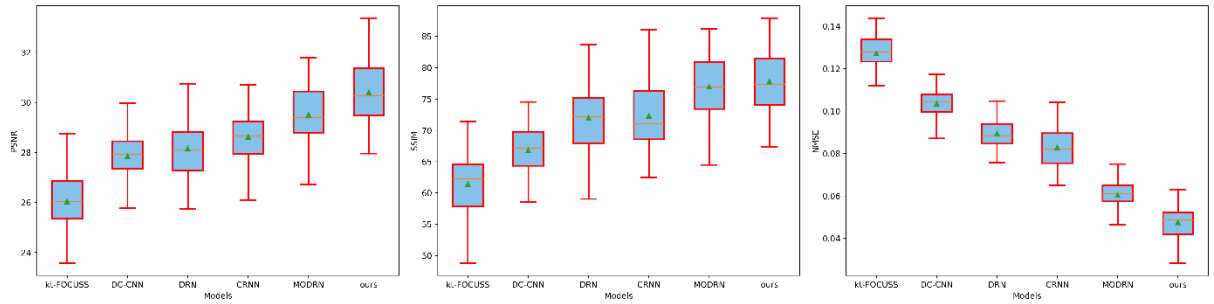


Figure 5. Boxplot of the distribution of quantitative results on the ACDC dataset under 8

\times acceleration.

The comparisons of visualization results of the reconstruction under $4 \times$ and $8 \times$ acceleration conditions are shown in Figures 6 and 7 respectively, with the reconstructed images, and their corresponding error maps using different methods on the ACDC dataset. As can be seen, the reconstructed results of the proposed method have best visual effects and least absolute errors relative to the ground truth compared with the other methods. The reconstructed images at the cardiac region of the proposed method have little artifacts and great details which benefit from the full utilization of spatial-temporal information in dynamic images.

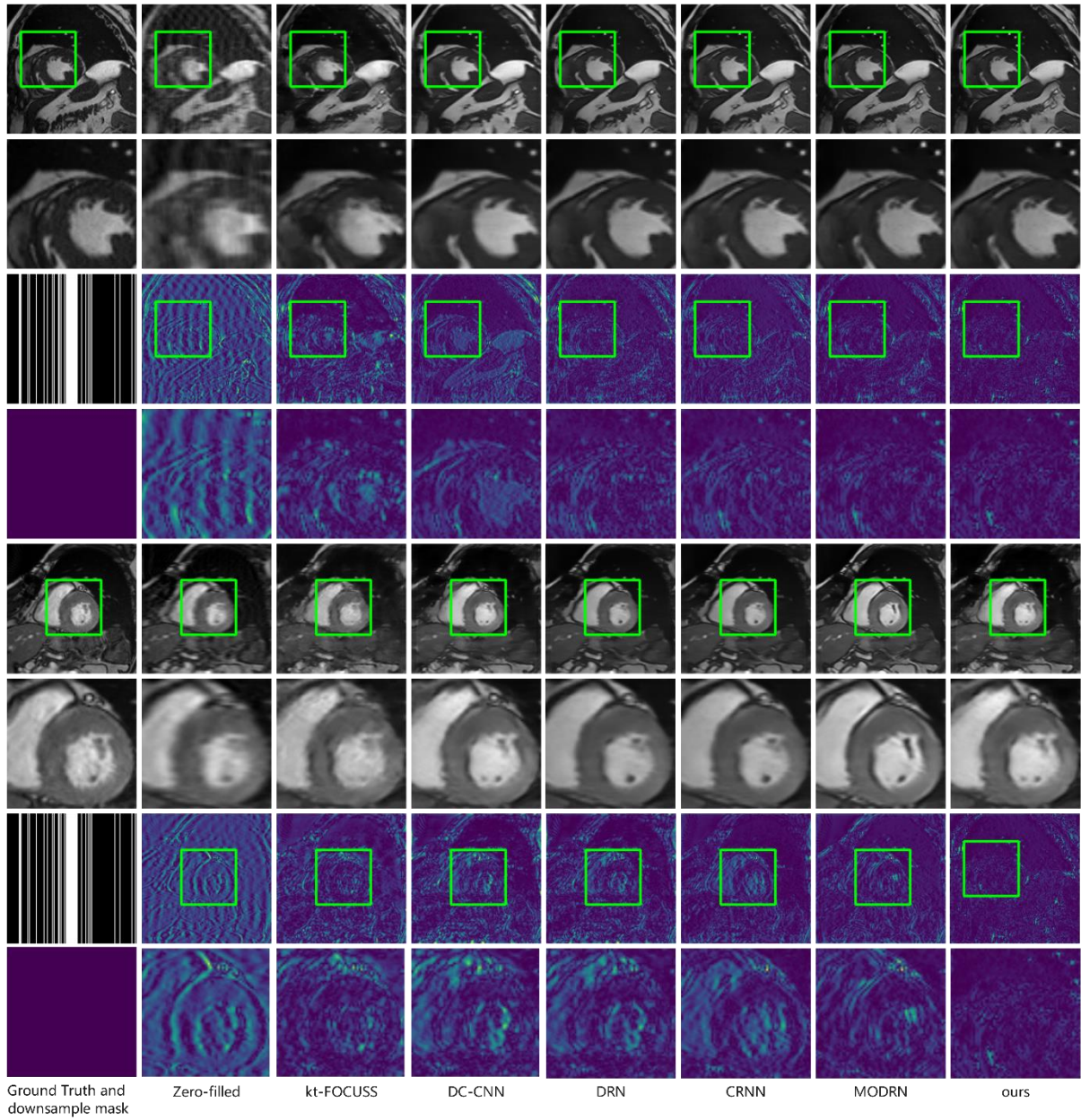


Figure 6. Qualitative results of different methods on the ACDC dataset under 4× acceleration.

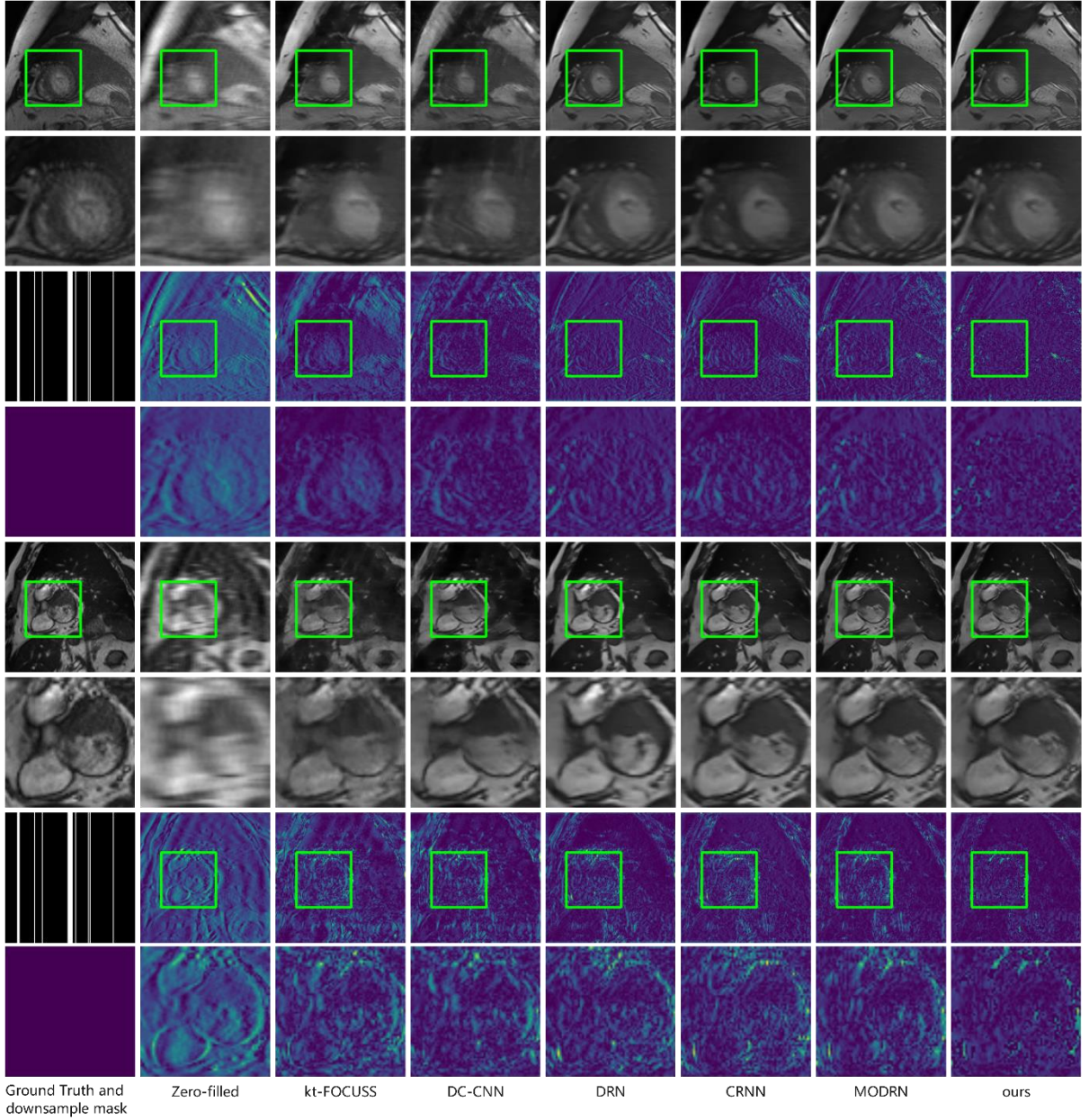


Figure 7. Qualitative results of different methods on the ACDC dataset under $8\times$ acceleration.

Furthermore, to verify the generalization of the proposed method, more comparison experiments are conducted on the SACMRI dataset under $4\times$ and $8\times$ acceleration conditions. The quantitative results of all methods under different acceleration factors are reported in Table 2. The proposed approach also outperforms other methods in terms of PSNR, SSIM, and NMSE values on the SACMRI dataset. Specifically, at a $4\times$ acceleration rate, the proposed method

improves 0.8% in SSIM and 0.94dB in PSNR compared with the suboptimal model MODRN.

At an $8\times$ acceleration rate, the proposed method improves 0.76% in SSIM and 0.61dB in PSNR relative to the suboptimal model MODRN. The visualizations of boxplot distribution about PSNR, SSIM, and NMSE under $4\times$ and $8\times$ acceleration rates are illustrated in Figures 8 and 9, respectively. The reconstructed images of different methods under $4\times$ and $8\times$ acceleration conditions on the SACMRI dataset are depicted in Figures 10 and 11, respectively. The proposed method surpasses other methods with excellent quantitative and qualitative results, which further verify the generalization and robustness.

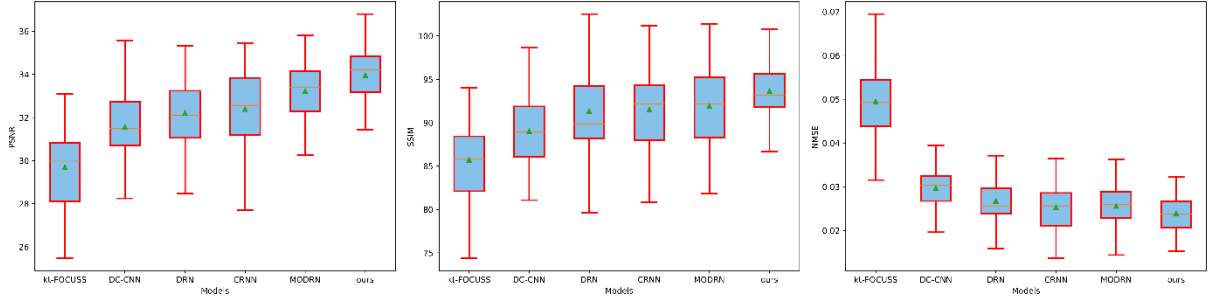


Figure 8. Boxplot of the distribution of quantitative results on the SACMRI dataset under $4\times$ acceleration.

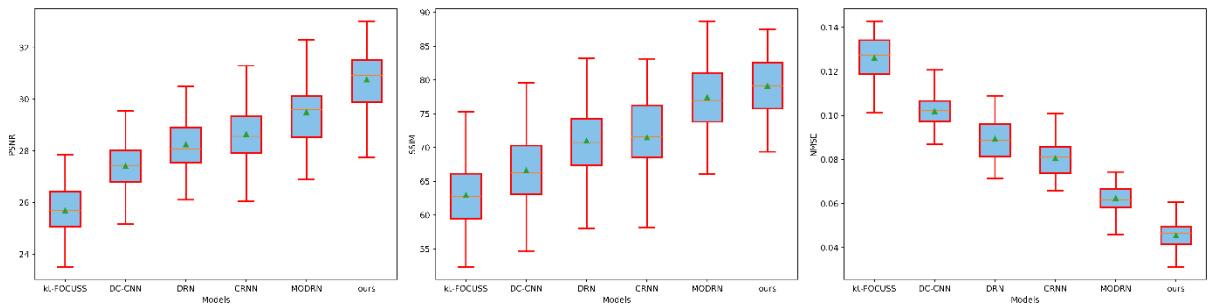


Figure 9. Boxplot of the distribution of quantitative results on the SACMRI dataset under $8\times$ acceleration.

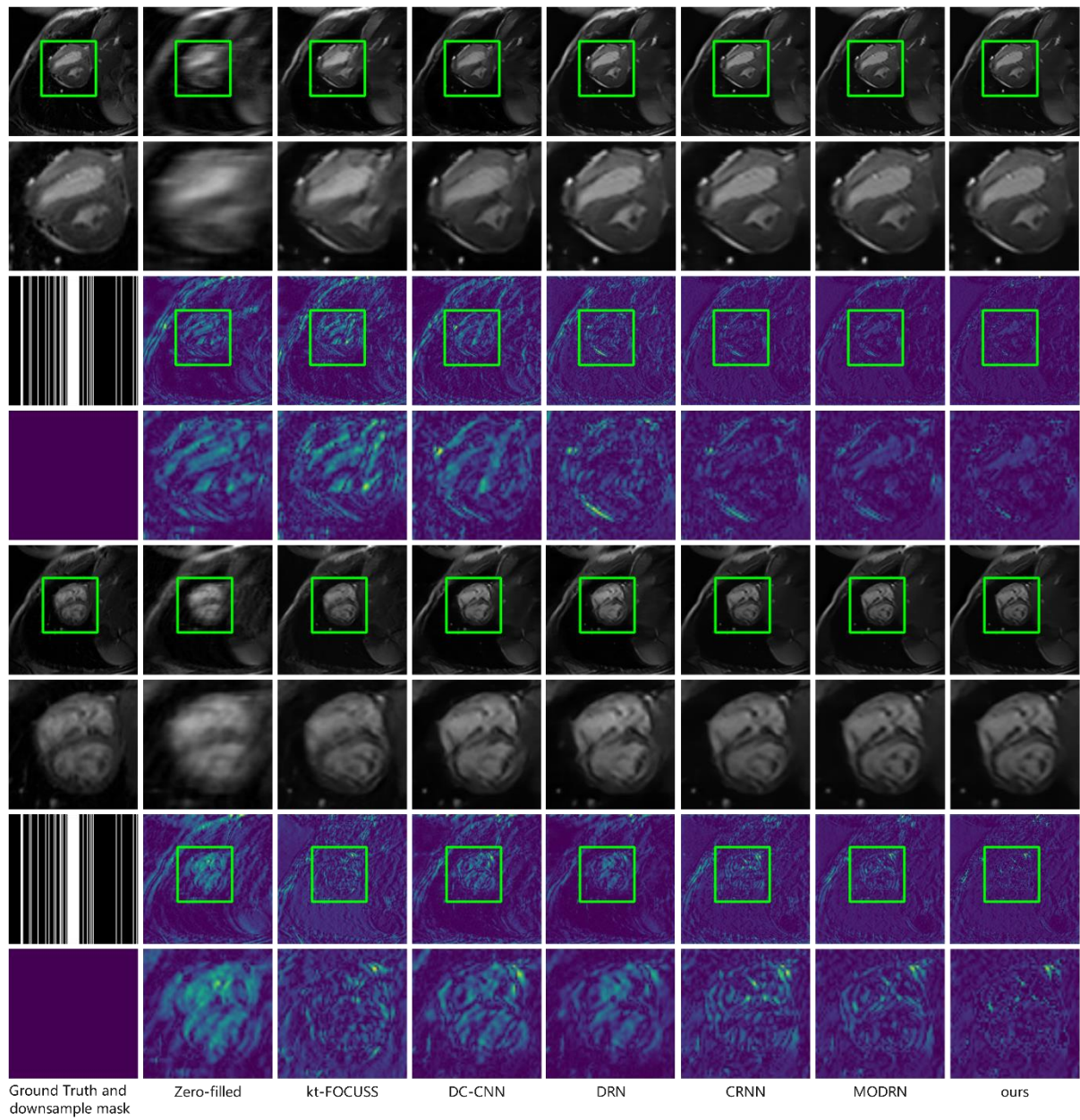


Figure 10. Qualitative results of different methods on the SACMRI dataset under 4× acceleration.

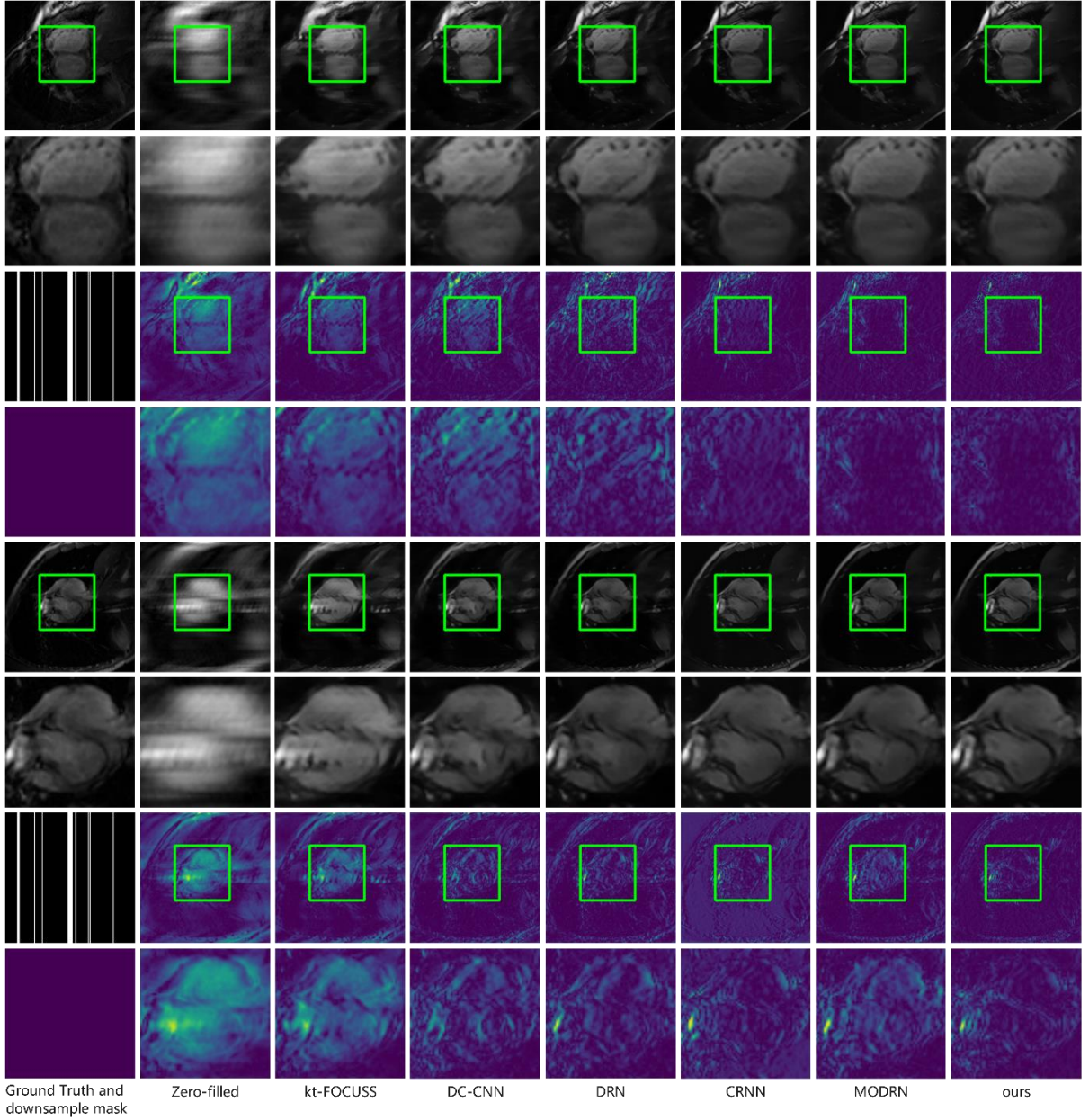


Figure 11. Qualitative results of different methods on the SACMRI dataset under 8× acceleration.

Ablation study

To demonstrate the feasibility and effectiveness of each component of the proposed network, three ablation studies are conducted based on the ACDC dataset. The first ablation study is to investigate the effectiveness of the MGDA and MRF modules whose compared results are listed in Table 3. Three metric values achieve the best performance by using both MGDA and MRF

modules. Furthermore, the analyses of t-test between the proposed method and the model only using MGDA module, and the proposed method and the model only using MRF module are conducted to explain of differences. The t-test results indicate that the removal of these modules significantly differs from each other ($p < 0.001$). MGDA compensates for motion artifacts in the current frame by capturing features from reference frames around, leading to a modest performance boost. Moreover, the potent feature fusion and artifact correction abilities of MRF contribute substantially to augmenting the model's reconstruction performance.

In the design MGDA module, second-order grid propagation (SOGP) strategy is adopted to aggregate more spatial-temporal information and improve the reconstruction performance. The second ablation study verifies the boosting ability between SOGP and first-order grid propagation (FOGP). As depicted in Table 4, SOGP facilitates the current frame in obtaining information from more different directional frames and exhibits greater competitiveness than FOGP. Additionally, the calculated t-test result can also demonstrate there is a significant difference between both cases ($p < 0.001$).

The last ablation study is about the architecture of the proposed MRF module, which consists of both CNN and Transformer. From Table 5, the experimental outcomes demonstrate that the performance is unsatisfactory when employing either CNN or Transformer in isolation, while the hybrid MRF architecture exhibits excellent performance. The t-test results between mutual two cases indicate that there are significant differences ($p < 0.001$).

Discussion

All experiments in terms of qualitative or quantitative results consistently demonstrate the superiority, robustness, and generalization of the proposed method. To reconstruct the clear

images with richer details and fewer artifacts from cardiac cine MRI, the proposed method designs MGAD and MRF modules based on the preliminary reconstructed results obtained using U-Net in k-space which can take full advantage of spatial-temporal characteristics of dynamic sequences. Meanwhile, the MGDA module uses DCN to align the adjacent cine MRI frames to eliminate the difference between these adjacent frames and remove the motion artifacts. In MGDA module, the second-order bidirectional propagation of SOGP strategy avoids the decay of alignment features from long-range alignments and acquires additional spatial positional features to refine detailed features. Finally, the MRF module effectively eliminates alignment errors, further removes the motion artifacts, and obtains the last reconstructed high-quality cardiac image.

Although the proposed method provides excellent results in dynamic cardiac cine reconstruction, it still has some limitations. First, the data used in the experiments are from public datasets and the under-sampled data are synthetic. Therefore, more real-world data from clinical will be collected to verify the proposed method in the future. Second, the network architecture of the proposed method is relatively complex and demands high computational resources. In future work, the complexity of the proposed method will be optimized to reduce computational costs.

Conclusion

A novel end-to-end network for cardiac cine MRI reconstruction under free breathing is proposed in this paper, intending to reconstruct high-quality cardiac images with minor errors at high acceleration factors. The proposed method first utilizes U-Net to reconstruct the initial cardiac images in k-space, and further designs two important modules, namely MGDA and

MRF to remove the motion artifacts to the greatest extent. Experimental results on two different datasets, i.e., ACDC and SACMRI, demonstrate that the proposed method has robust reconstruction performance under different acceleration rates. This study provides some guidance for cardiac cine MRI reconstruction.

Acknowledgments

The authors would like to thank the anonymous reviewers and the associate editor for their constructive comments and suggestions that helped to improve both the technical content and the presentation quality of this paper.

Grant Support

This work is supported by the National Natural Science Foundation of China under grant No. 61801288.

References

- [1] Patel M R, Klufas R A. Gradient-and spin-echo MR imaging of the brain. American Journal of Neuroradiology 1999; 20(7): 1381-1383.
- [2] Deshmane A, Gulani V, Griswold M A, et al. Parallel MR imaging. Journal of Magnetic Resonance Imaging 2012; 36(1): 55-72.
- [3] Lustig M, Donoho D, Pauly J M. Sparse MRI: The application of compressed sensing for rapid MR imaging. Magnetic Resonance in Medicine: An Official Journal of the International Society for Magnetic Resonance in Medicine 2007; 58(6): 1182-1195
- [4] Balachandrasekaran A, Ongie G, Jacob M. Accelerated dynamic MRI using structured low rank matrix completion. In: 2016 IEEE International Conference on Image Processing (ICIP). IEEE, 2016: 1858-1862.

- [5] Poddar S, Jacob M. Dynamic MRI using smoothness regularization on manifolds (SToRM). IEEE transactions on medical imaging 2015; 35(4): 1106-1115.
- [6] Wang S, Su Z, Ying L, et al. Accelerating magnetic resonance imaging via deep learning. In: 2016 IEEE 13th international symposium on biomedical imaging (ISBI). IEEE, 2016: 514-517.
- [7] Lee D, Yoo J, Tak S, et al. Deep residual learning for accelerated MRI using magnitude and phase networks. IEEE Transactions on Biomedical Engineering 2018; 65(9): 1985-1995.
- [8] Zhu B, Liu J Z, Cauley S F, et al. Image reconstruction by domain-transform manifold learning. Nature 2018; 555(7697): 487-492.
- [9] Xiang L, Chen Y, Chang W, et al. Deep-learning-based multi-modal fusion for fast MR reconstruction. IEEE Transactions on Biomedical Engineering 2018; 66(7): 2105-2114.
- [10] Han Y, Sunwoo L, Ye J C. k-space deep learning for accelerated MRI. IEEE transactions on medical imaging 2019; 39(2): 377-386.
- [11] Ran M, Hu J, Chen Y, et al. Denoising of 3D magnetic resonance images using a residual encoder–decoder Wasserstein generative adversarial network. Medical image analysis 2019; 55: 165-180.
- [12] Batchelor P G, Atkinson D, Irarrazaval P, et al. Matrix description of general motion correction applied to multishot images. Magnetic Resonance in Medicine: An Official Journal of the International Society for Magnetic Resonance in Medicine 2005; 54(5): 1273-1280.
- [13] Odille F, Vuissoz P A, Marie P Y, et al. Generalized reconstruction by inversion of coupled

- systems (GRICS) applied to free-breathing MRI. *Magnetic Resonance in Medicine: An Official Journal of the International Society for Magnetic Resonance in Medicine* 2008; 60(1): 146-157.
- [14] Chandarana H, Feng L, Ream J, et al. Respiratory motion-resolved compressed sensing reconstruction of free-breathing radial acquisition for dynamic liver MRI. *Investigative radiology* 2015; 50(11): 749.
- [15] Aviles-Rivero A I, Debroux N, Williams G, et al. Compressed sensing plus motion (CS+ M): a new perspective for improving undersampled MR image reconstruction. *Medical Image Analysis* 2021; 68: 101933.
- [16] Zhang T, Cheng J Y, Potnick A G, et al. Fast pediatric 3D free-breathing abdominal dynamic contrast enhanced MRI with high spatiotemporal resolution. *Journal of Magnetic Resonance Imaging* 2015; 41(2): 460-473.
- [17] Usman M, Ruijsink B, Nazir M S, et al. Free breathing whole-heart 3D CINE MRI with self-gated Cartesian trajectory. *Magnetic resonance imaging* 2017; 38: 129-137.
- [18] Schlemper J, Caballero J, Hajnal J V, et al. A deep cascade of convolutional neural networks for dynamic MR image reconstruction. *IEEE transactions on Medical Imaging* 2017; 37(2): 491-503.
- [19] Qin C, Schlemper J, Caballero J, et al. Convolutional recurrent neural networks for dynamic MR image reconstruction. *IEEE transactions on medical imaging* 2018; 38(1): 280-290.
- [20] Küstner T, Fuin N, Hammernik K, et al. CINENet: deep learning-based 3D cardiac CINE MRI reconstruction with multi-coil complex-valued 4D spatio-temporal convolutions.

Scientific reports 2020; 10(1): 13710.

- [21] Sarasaen C, Chatterjee S, Bretkopf M, et al. Fine-tuning deep learning model parameters for improved super-resolution of dynamic mri with prior-knowledge. *Artificial Intelligence in Medicine* 2021; 121: 102196.
- [22] Seegoolam G, Schlemper J, Qin C, et al. Exploiting motion for deep learning reconstruction of extremely-undersampled dynamic MRI. In: *Medical Image Computing and Computer Assisted Intervention–MICCAI 2019: 22nd International Conference, Shenzhen, China, October 13–17, 2019, Proceedings, Part IV*. Cham: Springer International Publishing, 2019: 704-712.
- [23] Huang Q, Xian Y, Yang D, et al. Dynamic MRI reconstruction with end-to-end motion-guided network. *Medical Image Analysis* 2021; 68: 101901.
- [24] Eldeniz C, Gan W, Chen S, et al. Phase2Phase: respiratory motion-resolved reconstruction of free-breathing magnetic resonance imaging using deep learning without a ground truth for improved liver imaging. *Investigative Radiology* 2021; 56(12): 809-819.
- [25] Pan J, Rueckert D, Küstner T, et al. Learning-based and unrolled motion-compensated reconstruction for cardiac MR CINE imaging. In: *International Conference on Medical Image Computing and Computer-Assisted Intervention*. Cham: Springer Nature Switzerland, 2022: 686-696.
- [26] Kunz J F, Ruschke S, Heckel R. Implicit Neural Networks with Fourier-Feature Inputs for Free-breathing Cardiac MRI Reconstruction. *arXiv preprint arXiv:2305.06822*, 2023.
- [27] Zucker E J, Sandino C M, Kino A, et al. Free-breathing accelerated cardiac MRI using deep learning: validation in children and young adults. *Radiology* 2021; 300(3): 539-548.

- [28] Biswas S, Aggarwal H K, Poddar S, et al. Model-based free-breathing cardiac MRI reconstruction using deep learned & storm priors: MoDL-storm. In: 2018 IEEE International Conference on Acoustics, Speech and Signal Processing (ICASSP). IEEE, 2018: 6533-6537.
- [29] Ronneberger O, Fischer P, Brox T. U-net: Convolutional networks for biomedical image segmentation. In: Medical Image Computing and Computer-Assisted Intervention—MICCAI 2015: 18th International Conference, Munich, Germany, October 5-9, 2015, Proceedings, Part III 18. Springer International Publishing, 2015: 234-241.
- [30] Tian Y, Zhang Y, Fu Y, et al. Tdan: Temporally-deformable alignment network for video super-resolution. In: Proceedings of the IEEE/CVF conference on computer vision and pattern recognition. 2020: 3360-3369.
- [31] Wang X, Chan K C K, Yu K, et al. Edvr: Video restoration with enhanced deformable convolutional networks. In: Proceedings of the IEEE/CVF Conference on Computer Vision and Pattern Recognition Workshops. 2019: 0-0.
- [32] Dai J, Qi H, Xiong Y, et al. Deformable convolutional networks. In: Proceedings of the IEEE international conference on computer vision. 2017: 764-773.
- [33] Chan K C K, Wang X, Yu K, et al. Understanding deformable alignment in video super-resolution. In: Proceedings of the AAAI conference on artificial intelligence. 2021, 35(2): 973-981.
- [34] Ranjan A, Black M J. Optical flow estimation using a spatial pyramid network. In: Proceedings of the IEEE conference on computer vision and pattern recognition. 2017: 4161-4170.

- [35] Chan K C K, Zhou S, Xu X, et al. Basicvsr++: Improving video super-resolution with enhanced propagation and alignment. In: Proceedings of the IEEE/CVF conference on computer vision and pattern recognition. 2022: 5972-5981.
- [36] Sun K, Xiao B, Liu D, et al. Deep high-resolution representation learning for human pose estimation. In: Proceedings of the IEEE/CVF conference on computer vision and pattern recognition. 2019: 5693-5703.
- [37] Vaswani A, Shazeer N, Parmar N, et al. Attention is all you need. Advances in neural information processing systems 2017; 30.
- [38] Liu Z, Lin Y, Cao Y, et al. Swin transformer: Hierarchical vision transformer using shifted windows. In: Proceedings of the IEEE/CVF international conference on computer vision. 2021: 10012-10022.
- [39] Bernard O, Lalande A, Zotti C, et al. Deep learning techniques for automatic MRI cardiac multi-structures segmentation and diagnosis: is the problem solved? IEEE transactions on medical imaging 2018; 37(11): 2514-2525.
- [40] Andreopoulos A, Tsotsos J K. Efficient and generalizable statistical models of shape and appearance for analysis of cardiac MRI. Medical image analysis 2008; 12(3): 335-357.
- [41] Schlemper J, Oktay O, Bai W, et al. Cardiac MR segmentation from undersampled k-space using deep latent representation learning. In: Medical Image Computing and Computer Assisted Intervention–MICCAI 2018: 21st International Conference, Granada, Spain, September 16-20, 2018, Proceedings, Part I. Springer International Publishing, 2018: 259-267.
- [42] Loshchilov I, Hutter F. Decoupled weight decay regularization. arXiv preprint

[43] Wang Z, Bovik A C, Sheikh H R, et al. Image quality assessment: from error visibility to structural similarity. IEEE transactions on image processing 2004; 13(4): 600-612.

[44] Jung H, Sung K, Nayak K S, et al. k-t FOCUSS: a general compressed sensing framework for high resolution dynamic MRI. Magnetic Resonance in Medicine: An Official Journal of the International Society for Magnetic Resonance in Medicine 2009; 61(1): 103-116.

Table 1. Quantitative comparison results on the ACDC dataset.

Method	4×			8×		
	PSNR(dB) ↑	SSIM(%) ↑	NMSE ↓	PSNR(dB) ↑	SSIM(%) ↑	NMSE ↓
zero-filled	26.39	63.88	0.0868	24.70	55.31	0.1532
kt FOCUSS	29.14±1.26	74.26±4.25	0.0651±0.0075	26.02±1.27	61.84±5.18	0.1273±0.0088
DC-CNN	31.79±1.17	81.90±4.16	0.0389±0.0031	27.62±1.15	67.21±4.92	0.1023±0.0074
DRN	33.29±1.36	86.03±4.34	0.0298±0.0071	28.22±1.34	71.31±5.63	0.0884±0.0091
CRNN	33.95±1.38	87.24±5.14	0.0281±0.0062	28.85±1.14	72.38±5.54	0.0819±0.0086
MODRN	34.28±1.29	88.04±4.36	0.0258±0.0076	29.54±1.26	76.69±5.18	0.0626±0.0062
MDAMF(ours)	35.06±1.19	89.40±4.13	0.0238±0.0048	30.46±1.22	78.40±4.57	0.0468±0.0075

Table 2. Quantitative comparison results on the ACMRI dataset.

Method	4×			8×		
	PSNR(dB) ↑	SSIM(%) ↑	NMSE ↓	PSNR(dB) ↑	SSIM(%) ↑	NMSE ↓
zero-filled	26.53	74.41	0.0871	25.15	56.94	0.1431
kt FOCUSS	29.48±1.79	86.26±4.58	0.0482±0.0075	26.79±1.54	78.56±5.12	0.0906±0.0085
DC-CNN	31.63±1.81	89.70±4.42	0.0287±0.0039	28.11±1.26	83.28±4.26	0.0798±0.0093
DRN	32.12±1.49	90.24±4.95	0.0272±0.0047	28.43±1.30	84.21±4.42	0.0664±0.0056
CRNN	32.42±1.62	91.08±5.13	0.0260±0.0051	28.98±1.44	85.11±4.83	0.0536±0.0042
MODRN	33.02±1.77	92.14±4.67	0.0248±0.0063	29.43±1.37	86.89±4.31	0.0496±0.0068
MDAMF(ours)	33.96±1.54	92.94±4.52	0.0235±0.0043	30.04±1.18	87.65±4.20	0.0473±0.0072

Table 3. Ablation study for verifying the effects of the MGDA and MRF module.

MGDA	MRF	4×			8×		
		PSNR(dB) ↑	SSIM(%) ↑	NMSE ↓	PSNR(dB) ↑	SSIM(%) ↑	NMSE ↓
✓	×	34.12	87.98	0.0256	28.92	74.04	0.0765
×	✓	34.45	88.27	0.0248	29.54	75.93	0.0687
✓	✓	35.06	89.40	0.0238	30.46	78.40	0.0468

Table 4. Ablation study for verifying the effects of the FOGP and SOGP of MGDA.

FOGP	SOGP	4×			8×		
------	------	----	--	--	----	--	--

		PSNR(dB) \uparrow	SSIM(%) \uparrow	NMSE \downarrow	PSNR(dB) \uparrow	SSIM(%) \uparrow	NMSE \downarrow
\checkmark	\times	34.86	88.48	0.0247	29.10	76.54	0.0598
\times	\checkmark	35.06	89.40	0.0238	30.46	78.40	0.0468

Table 5. Ablation study of different MRF architectures.

CNN	Trans	$4\times$			$8\times$		
		PSNR(dB) \uparrow	SSIM(%) \uparrow	NMSE \downarrow	PSNR(dB) \uparrow	SSIM(%) \uparrow	NMSE \downarrow
\checkmark	\times	34.57	88.90	0.0263	29.15	76.18	0.0608
\times	\checkmark	34.48	88.62	0.0258	29.29	76.40	0.0468
\checkmark	\checkmark	35.06	89.40	0.0238	30.46	78.40	0.0468